Introduction

Accurate estimates of the propagation velocities of seismic waves in the subsurface are utterly important in exploration geophysics. Seismic imaging requires a velocity model to reconstruct the Green functions in the medium and thus to map the reflected energy recorded at the surface back in the subsurface. Seismic velocities also carry information about the orientation of the principal stresses and overpressures (Carcione, 2007), which are important to plan drilling operations and assessing hazards. The estimation of the velocity model is usually performed in the framework of optimisation theory. The matching between observed and synthetic data generated in a trial model is evaluated using an objective function. The negative of the gradient of the objective function indicates the direction in which the trial model must be updated to decrease the objective function and increase the similarity between the two datasets. If the observed and synthetic data are compared directly, the algorithm is usually referred to as waveform inversion (WI) (Tarantola, 1984; Pratt, 1999); if the data are first remapped in the depth domain and consistency between seismic images is evaluated, the method is called migration velocity analysis (MVA) (Faye and Jeannot, 1986; Al-Yahya, 1989; Sava and Biondi, 2004). WI is simple to implement and can reconstruct high-resolution velocity models but requires an accurate parametrization of the physics of wave propagation, knowledge of the source signature, and a kinematically reliable starting model in order to converge to the global minimum of the objective function (Santosa and Symes, 1989). MVA is more robust against errors in the initial velocity model and its objective function is convex over a wide range of model perturbations, thus more suitable for gradient-based optimisation. Nonetheless, MVA does not use the amplitude information in the data and cannot achieve the high-resolution results that WI promises in the ideal scenario. Here, we compare seismic images obtained from different shots using image-warping and implement a MVA scheme based on standard differential semblance optimisation (DSO). Image-warping appears to be more robust than both standard DSO and penalized local-correlations (Perrone and Sava, 2012) for measuring consistency between migrated images.

Theory

DSO in the shot-image domain minimizes the energy of the difference of nearby images (Symes, 1993):

$$\mathcal{J}_{DSO}\left(m\right) = \frac{1}{2}\sum_{i}\left\|R_{i+1} - Ri\right\|^{2}, \tag{1}$$

where $R_i\left(\mathbf{x}\right)$ is the migrated image obtained from the ith shot, $m\left(\mathbf{x}\right)$ represents the model parameter, and $\mathbf{x} = \left(x, y, z\right)$ is the position vector. Perrone et al. (2014) show that the objective function in equation 1 can be approximated using image-warping as

$$\mathcal{J}_{WARP}\left(m\right) = \frac{1}{2}\sum_{i}\left\|\nabla R_i \cdot \mathbf{u}_i\right\|^{2}, \tag{2}$$

where $\mathbf{u}_i\left(\mathbf{x}\right)$ is the displacement vector field that maps R_i into R_{i+1} and ∇R_i is the gradient of the migrated image. Perrone et al. (2014) solve the optimisation problem through a series of linearized problems, where the tomographic operator is derived from the one-way migration operator. Displacement vectors $\mathbf{u}$ are obtained by an iterative search of the maximum of local correlations and warping of the input images; the algorithm is the one used for measuring the apparent shift between migrated images in 4D seismic processing (Hale, 2009). The displacement vector field is such that $R_i\left(\mathbf{x}+\mathbf{u}\right) = R_{i+1}\left(\mathbf{x}\right)$, and is obtained by computing the correlation lag that maximizes the local correlations $\mathbf{u}\left(\mathbf{x}\right) = \arg\max_{\boldsymbol{\lambda}} c\left(\mathbf{x},\boldsymbol{\lambda}\right)$, where $c\left(\mathbf{x},\boldsymbol{\lambda}\right) = \int_{w(\mathbf{x})} R_i\left(\boldsymbol{\xi} - \frac{\boldsymbol{\lambda}}{2}\right) R_{i+1}\left(\boldsymbol{\xi} + \frac{\boldsymbol{\lambda}}{2}\right) d\boldsymbol{\xi}$ is the local correlation of two images $R_i\left(\mathbf{x}\right)$ and $R_{i+1}\left(\mathbf{x}\right)$, and $w\left(\mathbf{x}\right)$ are seamlessly overlapping windows. Perrone and Sava (2012) use penalized local correlations between migrated images to measure the shift normal to the reflector. Adjoint-state calculations for the objective function in equation 2 can be performed using connective functions (Luo and Schuster, 1991). Here, we obtain a simpler tomographic algorithm by strengthening conventional DSO using image-warping. The adjoint sources $g_{si}\left(\mathbf{x},t\right) = \left(R_{i-1} - 2R_i + R_{i+1}\right) u_{ri}$ and $g_{ri}\left(\mathbf{x},t\right) = \left(R_{i-1} - 2R_i + R_{i+1}\right) u_{si}$ for DSO objective function depend on the second derivative of the migrated images along the shot axis and the source and receiver wavefields $u_{si}\left(\mathbf{x},t\right)$ and

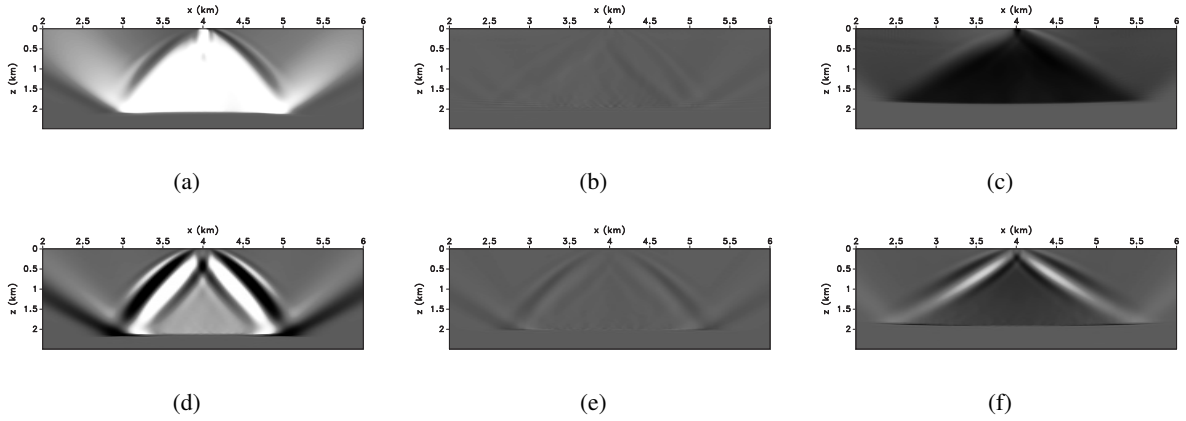

Figure 1: Sensitivity kernels for a *deep interface* using *image warping* for (a) high, (b) correct, and (c) low velocities, and using *differential semblance* for (d) high, (e) correct, and (f) low velocities.

$u_{ri}(\mathbf{x},t)$ in the background model (Plessix, 2006) and are the force terms for the adjoint wave-equations $\mathcal{L}(m)\, a_{si} = g_{si},\ \mathcal{L}(m)\, a_{ri} = g_{ri}$, where $a_{si}(\mathbf{x},t)$ and $a_{ri}(\mathbf{x},t)$ are the adjoint wavefields and $\mathcal{L}(m)$ is the d'Alembert operator. The adjoint-sources generate the scattered fields due to the reflectivity perturbation $(R_{i-1} - 2R_i + R_{i+1})$. The gradient of the objective function is the zero-lag time correlation of the background and adjoint wavefields (Plessix, 2006). Cycle skipping arises when, because of errors in the velocity model, different images map the same structures at inconsistent positions in the subsurface. We replace the term $(R_{i-1} - 2R_i + R_{i+1})$ with an approximation derived from image-warping. The apparent displacement field removes the cycle skipping problem by warping one image into its neighbour. Let us indicate with $\mathbf{u}_i^-$ and $\mathbf{u}_i^+$ the apparent displacement fields that warp R_i into R_{i-1} and R_i into R_{i+1}, respectively. An approximation of the image difference is the dot product of the image gradient and displacement field (Perrone et al., 2014). To guarantee symmetry with respect to the ith shot, we use R_i to construct the image perturbations

$$\Delta R_i^- = R_{i-1} - R_i \approx \nabla R_i \cdot \mathbf{u}_i^-,\ \Delta R_i^+ = R_{i+1} - R_i \approx \nabla R_i \cdot \mathbf{u}_i^+. \tag{3}$$

Using the expressions in equations 3, we can write

$$R_{i-1} - 2R_i + R_{i+1} \approx \Delta R_i^- + \Delta R_i^+, \tag{4}$$

which is robust against cycle skipping because only one image R_i enters the expression of the image perturbation and the warping vector $\mathbf{u}$ accounts for the shifts between images.

Numerical examples

Let us consider a horizontal reflector due a density contrast at 2 km depth in a homogeneous velocity model. We analyze 2 nearby shots: the first shot is at $x = 3.8$ km and the shot separation is 200 m. The rows (top to bottom) of Figure 1 show the sensitivity kernels obtained from image-warping and DSO wavefield tomography, respectively. The columns (left to right) show the results for a velocity model that is too fast, correct, and too slow, respectively. Image warping resolves the cycle-skipping between the migrated images that causes the strong sidelobes in differential semblance and allows one to obtain smoother sensitivity kernels. Figure 2 shows the comparison of image-warping and penalized local correlations wavefield tomography (top and bottom row, respectively) for a shallower interface at 1 km depth. The model perturbations applied to the velocity field are the same used in the previous case. The position of the first shot is again at $x = 3.8$ km and the shot separation is 200 m. Penalized local correlations suffer from the strong bias at the edges of the aperture, where the two images do not overlap. Image warping returns kernels with the correct sign even when the interface is closer to the surface and cycle skipping problems arise from the difference between the apertures of the two shots.

We also model 100 shots every 80 m of the Marmousi model. The spatial sampling is 8 m in both

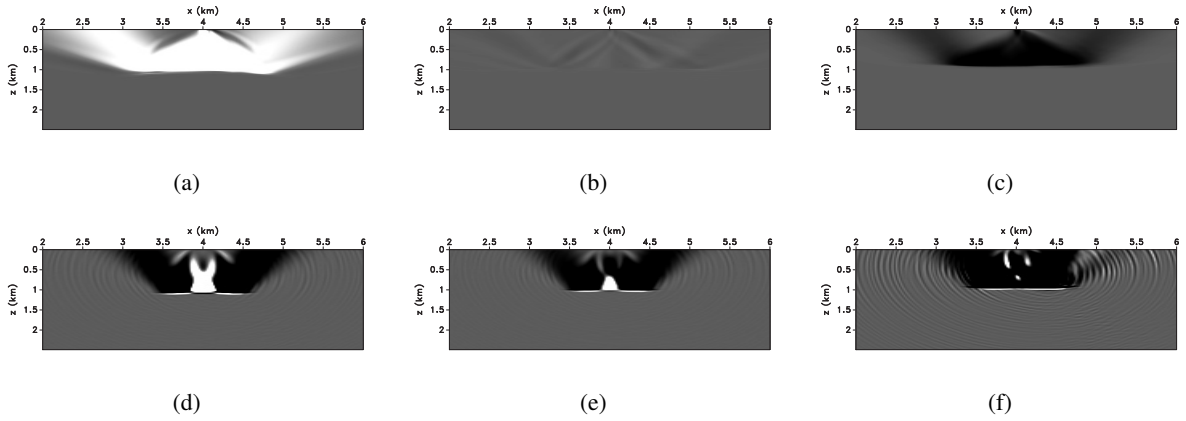

Figure 2: Sensitivity kernels for a *shallow interface* using *image warping* for (a) high, (b) correct, and (c) low velocities, and using *penalized local correlations* for (d) high, (e) correct, and (f) low velocities.

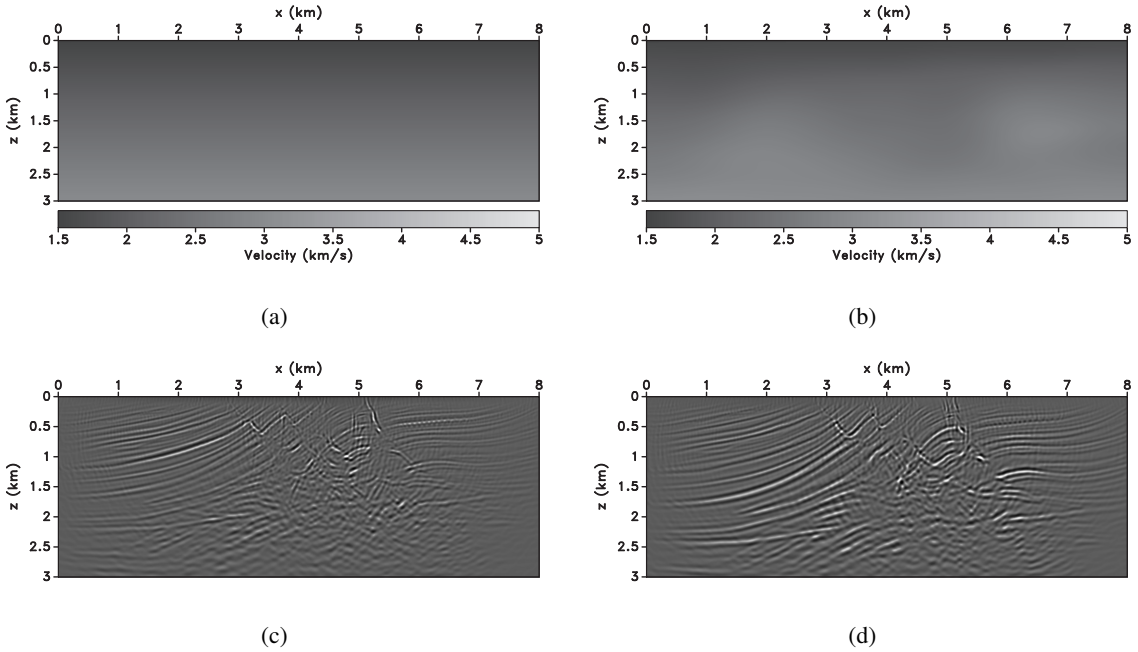

Figure 3: (a) The initial incorrect $v(z)$ velocity model and (b) the corresponding migrated image. (c) Recovered velocity model and (d) migrated image using the result of the inversion.

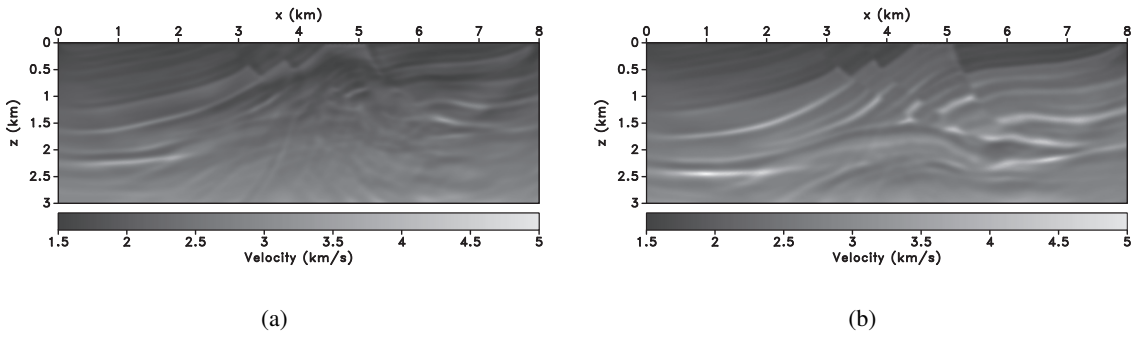

Figure 4: Full-waveform inversion result obtained using (a) the initial model for image-domain tomography and (b) the image-warping wavefield tomography inverted model in Figure 3(b) as initial guess.

spatial directions. Receivers are located at every grid point on the surface. The data are modeled without free-surface multiples but internal multiples are present. The initial model is the vertical gradient of velocity in Figure 3(a) and is slower than the trend in the correct model. The migrated image using the initial model is shown in Figure 3(c). Most reflectors are mispositioned, e.g. the deep and strong reflectors are shifted about 500 m upward. The complex wave propagation, the strong refractions, and the internal multiples contribute noise and artefacts in the migrated image due to the incorrect mapping of the scattered energy back in the subsurface. We implement a steepest-descent algorithm with parabolic line-search and reconstructs the smooth background velocity model in Figure 3(b), which is characterised by a steeper velocity gradient than the model in Figure 3(a). Figure 3(d) shows that image-warping wavefield tomography better positions reflectors where the geology is simple and the geometrical features of the image can be precisely computed. However, the high level of coherent noise in the partial images quickly decreases the quality of the image in the faulted portion of the model. We test the MVA result by running a WI test. The model in Figure 3(a) does not have the correct velocity gradient and leads to evident cycle-skipping in the WI result, as shown in Figure 4(a). The model reconstructed by image-warping wavefield tomography contains long-wavelength components that allow WI to converge to the result in Figure 4(b). The data used for the WI are low-passed filtered with a cut-off frequency of 3 Hz.

Conclusions

Image-warping represents a more robust version of shot-based DSO wavefield tomography. The displacement vector field warps a migrated image into the image obtained from a neighboring experiment and removes cycle-skipping because every reflector in one image is mapped into the corresponding event in the second image. Image-warping is more effective than penalized local image correlation wavefield tomography when the ratio between the source separation and the depth of the reflector is high. The Marmousi test shows that image-warping wavefield tomography can correct strong errors in the velocity model where the geometry of the reflectors is simple. The result of image-warping wavefield tomography is a suitable initial model for higher-resolution techniques.

REFERENCES

Al-Yahya, K., 1989, Velocity analysis by iterative profile migration: Geophysics, **54**, P. 718–729.

Carcione, J., 2007, Wave fields in real media wave propagation in anisotropic, anelastic, porous and electromagnetic media: Elsevier. Handbook of Geophysical Exploration.

Faye, J.-P., and J.-P. Jeannot, 1986, Prestack migration velocity analysis from focusing depth imaging: Presented at the 56th Annual International Meeting, SEG.

Hale, D., 2009, A method for estimating apparent displacement vectors from time-lapse seismic images: Geophysics, **74**, V99 – V107.

Luo, Y., and G. T. Schuster, 1991, Wave-equation traveltime inversion: Geophysics, **56**, 645–653.

Perrone, F., and P. Sava, 2012, Wavefield tomography based on local image correlation: 74th Conference and Exhibition, EAGE, Extended Abstracts.

Perrone, F., P. Sava, C. Andreoletti, and N. Bienati, 2014, Linearized wave-equation migration velocity analysis by image warping: Geophysics, **in press**.

Plessix, R.-E., 2006, A review of the adjoint-state method for computing the gradient of a functional with geophysical applications: Geophys. J. Int., **167**, 495–503.

Pratt, R. G., 1999, Seismic waveform inversion in the frequency domain, Part 1: Theory and verification in a physical scale model: Geophysics, **64**, 888–901.

Santosa, F., and W. W. Symes, 1989, An analysis of least-squares velocity inversion, *in* Geophysical Monograph no. 4: Society of Exploration Geophysicists.

Sava, P., and B. Biondi, 2004, Wave-equation migration velocity analysis. I. Theory: Geophysical Prospecting, **52**, 593–606.

Symes, W. W., 1993, A differential semblance criterion for the inversion of multioffset seismic reflection data: Journal of Geophysical Research, **98**, 2061 –2073.

Tarantola, A., 1984, Inversion of seismic reflection data in the acoustic approximation: Geophysics, **49**, 71–92.